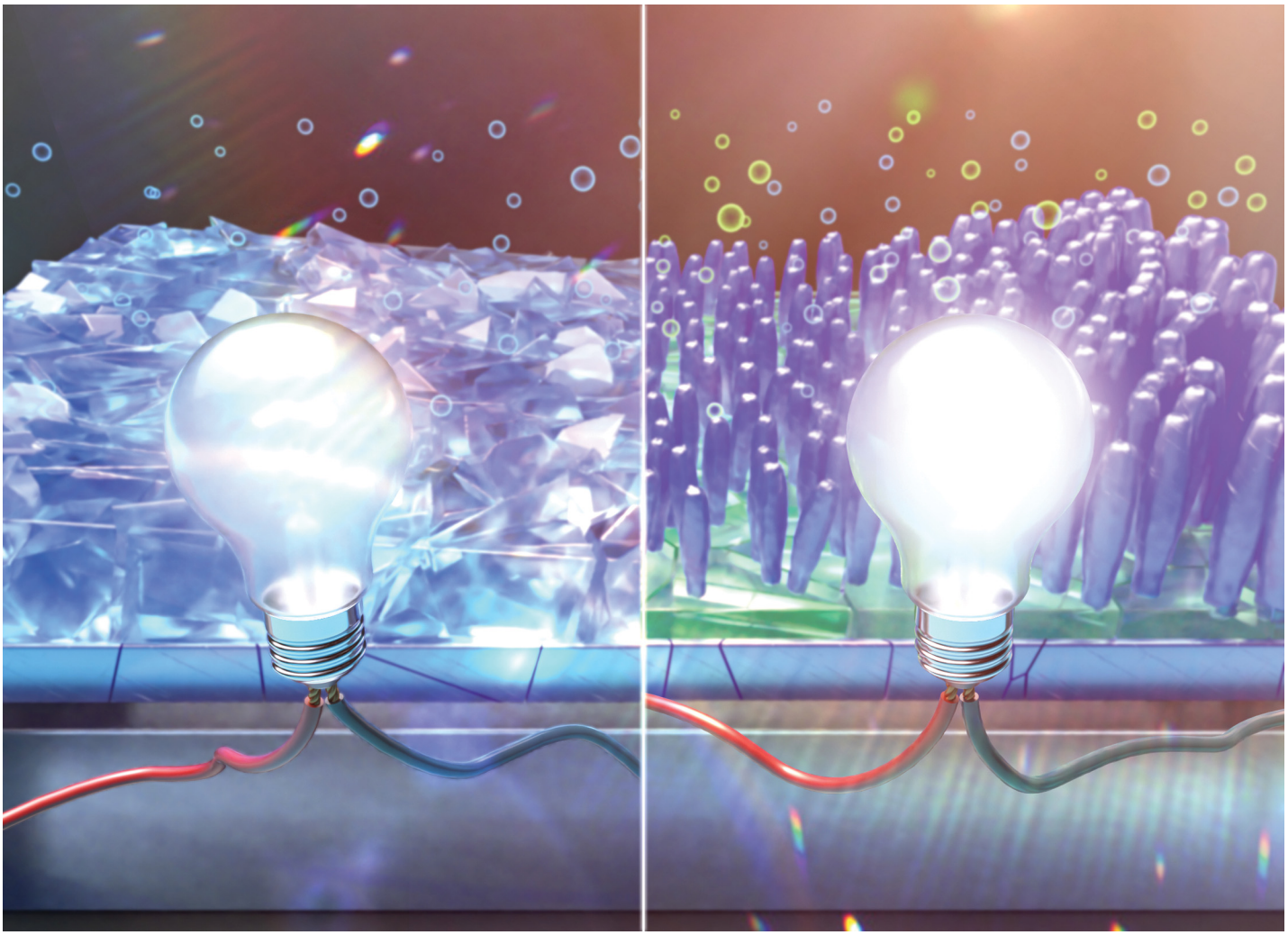

Showcasing research from Dr Kim & Dr Sung's Group, Division of Energy Technology, Convergence Research Institute, DGIST, Daegu, Korea.

Facile growth of a Sb_2Se_3 nanorods array induced by a $MoSe_2$ interlayer and its application in 3D p–n junction solar cells

Co-evaporation process was used to deposit uniformly grown Sb_2Se_3 nanorods array using a $MoSe_2$ interlayer. The $MoSe_2$ interlayer acted as a crucial role as a seed layer for the preferential growth of the Sb_2Se_3 nanorods and also improved the contact quality between the Sb_2Se_3 nanorods array and a Mo substrate. The application of the Sb_2Se_3 nanorods array to 3D p–n junction high-efficiency Sb_2Se_3 solar cells was also presented.

As featured in:

See Shi-Joon Sung, Dae-Hwan Kim *et al.*, *Mater. Adv.*, 2022, **3**, 978.

ROYAL SOCIETY OF CHEMISTRY

rsc.li/materials-advances

Registered charity number: 207890

Materials Advances

ROYAL SOCIETY OF CHEMISTRY

PAPER

View Article Online
View Journal | View Issue

Cite this: *Mater. Adv.*, 2022, 3, 978

Facile growth of a Sb_2Se_3 nanorod array induced by a $MoSe_2$ interlayer and its application in 3D p–n junction solar cells†

Si-Nae Park,‡[a] Se-Yun Kim,‡[b] Sang-Ju Lee,[ac] Shi-Joon Sung, *[ac] Kee-Jeong Yang,[ac] Jin-Kyu Kang[ac] and Dae-Hwan Kim *[ac]

A uniformly grown Sb_2Se_3 nanorod array, with the introduction of a $MoSe_2$ interlayer, obtained by a co-evaporation process and its application in three-dimensional (3D) p–n junction high-efficiency Sb_2Se_3 solar cells were investigated in this study. The $MoSe_2$ interlayer played a crucial role as a seed layer for the preferential growth of Sb_2Se_3 crystals, which facilitated the formation of a Sb_2Se_3 nanorod array regardless of the process conditions. 3D p–n junction between the Sb_2Se_3 nanorod array and the CdS buffer layer improved the short-circuit current of Sb_2Se_3 solar cells due to improved carrier transportation from the Sb_2Se_3 absorber to the CdS buffer. The $MoSe_2$ interlayer also improved the contact quality between the Sb_2Se_3 nanorod array and the Mo substrate by forming a quasi-ohmic contact, which resulted in a higher open-circuit voltage due to a reduced contact barrier and series resistance in Sb_2Se_3 solar cells. The crystal growth rate of Sb_2Se_3 was controlled by the source evaporation rate and substrate temperature to tune the final nanostructure and crystalline orientation of the co-evaporated Sb_2Se_3 nanorods array. 3D p–n junction solar cells based on an ordered and (*hk*1) preferentially oriented Sb_2Se_3 nanorod array showed a power conversion efficiency of 5.637%. Therefore, by including a $MoSe_2$ interlayer, it is possible to achieve high-efficiency 3D p–n junction Sb_2Se_3 solar cells.

Received 3rd September 2021,
Accepted 19th December 2021

DOI: 10.1039/d1ma00804h

rsc.li/materials-advances

Introduction

Antimony selenide (Sb_2Se_3) is one of the most promising semiconductor materials for thin-film solar cells because of its outstanding optoelectronic properties. Additionally, it is a non-toxic, relatively low-cost material with high absorption coefficient and low processing temperature.[1–6] Therefore, significant research has been conducted in the past decade to replace the conventional multinary compound semiconductors in thin-film solar cells for Sb_2Se_3.[7–11] However, the best power conversion efficiency (PCE) reported so far for Sb_2Se_3 solar cells is approximately 10%,[12] which is similar to those of thin-film solar cells made of conventional materials. In order to overcome the efficiency limitation of the Sb_2Se_3 solar cells, the application of three-dimensional (3D) nanostructured Sb_2Se_3 thin films for the formation of the 3D p–n junction solar cells could be one of the promising solutions.[13–15]

Carrier transportation and p–n junction formation in Sb_2Se_3 solar cells are closely related to the Sb_2Se_3 nanostructure. Therefore, the latter is one of the critical factors determining the photovoltaic performance of Sb_2Se_3 solar cells. However, there is little study on the nanostructure control of the Sb_2Se_3 thin films for high efficiency solar cells. Li *et al.* improved the short-circuit current (J_{SC}) of a solar cell using a 1000 nm-high Sb_2Se_3–nanorod array with superior light-harvesting capacity and reduced optical reflection.[16] In our previous work, we investigated the evolution of Sb_2Se_3 nanorods by controlling the process temperature of co-evaporation and proposed the photovoltaic performance enhancement of Sb_2Se_3 solar cells based on 3D p–n junction formation.[18] However, the temperature window for the formation of Sb_2Se_3 nanorods was narrow and the orientation of the Sb_2Se_3 nanorods was random. From these previously reported studies, it was found that the application of 3D nanostructured Sb_2Se_3 absorber layers would be very useful to overcome of the performance limitation of Sb_2Se_3 solar cells based on the 3D p–n junction solar cell concept. However, to the best of the authors' knowledge, there is no detailed investigation of the nanostructure evolution of Sb_2Se_3 thin films reported in the literature.

[a] *Research Center for Thin Film Solar Cells, Daegu-Gyeongbuk Institute of Science and Technology (DGIST), Daegu 42988, Republic of Korea. E-mail: sjsung@dgist.ac.kr, monolith@dgist.ac.kr*
[b] *Department of Materials Science and Engineering, Kyungnam University, Geyongsangnam-do 51767, Republic of Korea*
[c] *Division of Energy Technology, Daegu-Gyeongbuk Institute of Science and Technology (DGIST), Daegu 42988, Republic of Korea*

† Electronic supplementary information (ESI) available. See DOI: 10.1039/d1ma00804h

‡ These authors contributed equally to this paper.

The objective of this work was to study the evolution of a nanostructured Sb_2Se_3 thin film fabricated using a $MoSe_2$ interlayer and the co-evaporation process. Additionally, a detailed investigation of the controlling factor to achieve fine-tuned Sb_2Se_3 nanorod arrays is presented in this work. In our work, we proposed the evolution of nanostructured Sb_2Se_3 thin films using a $MoSe_2$ interlayer and detailed investigation on the control factor of the co-evaporation process for the fine-tuning of the Sb_2Se_3 nanorod array. By introducing a $MoSe_2$ interlayer between the Mo substrate and Sb_2Se_3, it was possible to form uniformly ordered packed Sb_2Se_3 nanorod formation using co-evaporation of Sb_2Se_3 and Se sources. The $MoSe_2$ interlayer has locally distributed dangling bonds, which play the role of nucleation seed for Sb_2Se_3 crystalline growth perpendicular to the Mo substrate. Because of the seeding effect of the $MoSe_2$ interlayer, Sb_2Se_3 thin films deposited on the $MoSe_2$ interlayer dominantly showed a uniformly ordered packed Sb_2Se_3 nanorod array. In addition, the formation of a quasi-ohmic contact between Sb_2Se_3 and $MoSe_2$ was another improving point of open-circuit voltage (V_{OC}) of Sb_2Se_3 solar cells compared with Sb_2Se_3 solar cells without the $MoSe_2$ interlayer.

The nanostructure of the Sb_2Se_3 nanorod arrays on the $MoSe_2$ interlayer was also sensitively affected by the conditions of the co-evaporation processes, such as the evaporation rate of sources and substrate temperature. The growth behavior of Sb_2Se_3 crystals during the co-evaporation process was closely related with the final nanostructure of Sb_2Se_3 nanorod array, which was the main factor that determines the short-circuit current (J_{SC}) of Sb_2Se_3 solar cells. The crystalline orientation of co-evaporated Sb_2Se_3 thin films, which is a crucial factor for high efficiency Sb_2Se_3 solar cells, was also affected by the substrate temperature.[18–25] After chemical bath deposition (CBD) of n-type CdS buffer layers on the Sb_2Se_3 nanorod array, the 3D p–n junction between Sb_2Se_3 and CdS was formed and the 3D p–n junction was effective for the enhancement of J_{SC}. By introducing the $MoSe_2$ interlayer, the growth of a uniformly ordered Sb_2Se_3 nanorod array and the quasi-ohmic contact between Sb_2Se_3 and $MoSe_2$ were possible and 3D p–n junction Sb_2Se_3 solar cells with 5.637% efficiency was achieved.

Experimental

$MoSe_2$ interlayer and Sb_2Se_3 thin-film preparation

The structure of the studied Sb_2Se_3 thin films consisted of a soda-lime glass (SLG) substrate and a 600 nm-thick Mo layer as the back-contact layer. Before deposition, the substrate was sequentially cleaned in an ultrasonic bath using acetone, methanol, and deionized water. The Mo layer was deposited on the SLG substrate *via* direct current (DC) magnetron sputtering using a Mo target with a purity of 99.99%.

To form the $MoSe_2$ interlayer on Mo substrates, the latter were treated in a tube furnace in a Se atmosphere. Vacuum (10^{-3} Torr) was applied to the furnace to remove moisture and impurities. Then, Ar gas was introduced into the furnace, allowing the pressure inside the furnace to reach the atmospheric pressure. The furnace was heated to 430 °C with Se pellets inside for 10 min and then annealed for 10 min. The $MoSe_2$ layer obtained was approximately 100 nm-thick.

The Sb_2Se_3 thin films were prepared on bare Mo substrates or $MoSe_2$/Mo substrates using a co-evaporator system using Sb_2Se_3 and Se sources. The substrate temperature was controlled in the range of 250–290 °C. The substrate was heated at 0.53 °C s^{-1} from room temperature (~25 °C) to the desired temperature. The evaporation rate of Sb_2Se_3 and Se sources varied from 50–200 Å s^{-1}. Sb_2Se_3 was deposited to obtain thin films (thickness: approximately 500 nm). After deposition, the samples were allowed to cool to room temperature naturally.

Solar cell fabrication

Chemical bath deposition (CBD) was used to cover the Sb_2Se_3 thin films obtained with a 50 nm-thick n-type cadmium sulfide (CdS) buffer layer, and radiofrequency (RF) sputtering was used to sequentially deposit a 50 nm-thick intrinsic ZnO window layer and a 300 nm-thick Al-doped ZnO (AZO) A transparent conducting oxide (TCO) layer was deposited on top of the buffer layer to fabricate the solar cells. Thermal evaporation was then used to deposit a 1 μm-thick Al collection grid on top of the device.

Characterization of Sb_2Se_3 solar cells

The Sb_2Se_3 thin films were analyzed using various techniques to determine the influence of substrate temperature on the chemical composition and morphology of the films, and consequently, on the photovoltaic characteristics of the Sb_2Se_3 solar cells. The surface morphology and chemical composition of the Sb_2Se_3 thin films were observed using field emission scanning electron microscopy (FE-SEM, Hitachi, SU8020) and transmission electron microscopy (FE-TEM, Hitachi, HF-3300) with a focused ion beam (FIB) system (Hitachi, NB 5000). The crystalline structure of the Sb_2Se_3 thin films was determined using X-ray diffraction (XRD) analysis (Panalytical, Empyrean). The photovoltaic characteristics of the solar cells were characterized using a source meter (Keithley, 2400) unit and a solar simulator (Newport, 94022A) to simulate 1.5AM solar irradiation.

Results and discussion

To obtain a controlled Sb_2Se_3 crystalline structure in Sb_2Se_3 solar cells, an $MoSe_2$ interlayer between the Sb_2Se_3 absorber and the Mo substrate was adopted. Additionally, the $MoSe_2$ interlayer between Sb_2Se_3 and the Mo substrate played an important role in the growth control of the Sb_2Se_3 crystalline structure. To investigate the role and effect of the $MoSe_2$ interlayer on Sb_2Se_3 crystal growth, Sb_2Se_3 thin films were deposited on bare Mo substrates and $MoSe_2$/Mo substrates using the co-evaporation process at different source evaporation rates (50–200 Å s^{-1}). The source evaporation rate is closely related to the Sb_2Se_3 crystal growth mechanism. Fig. 1 shows

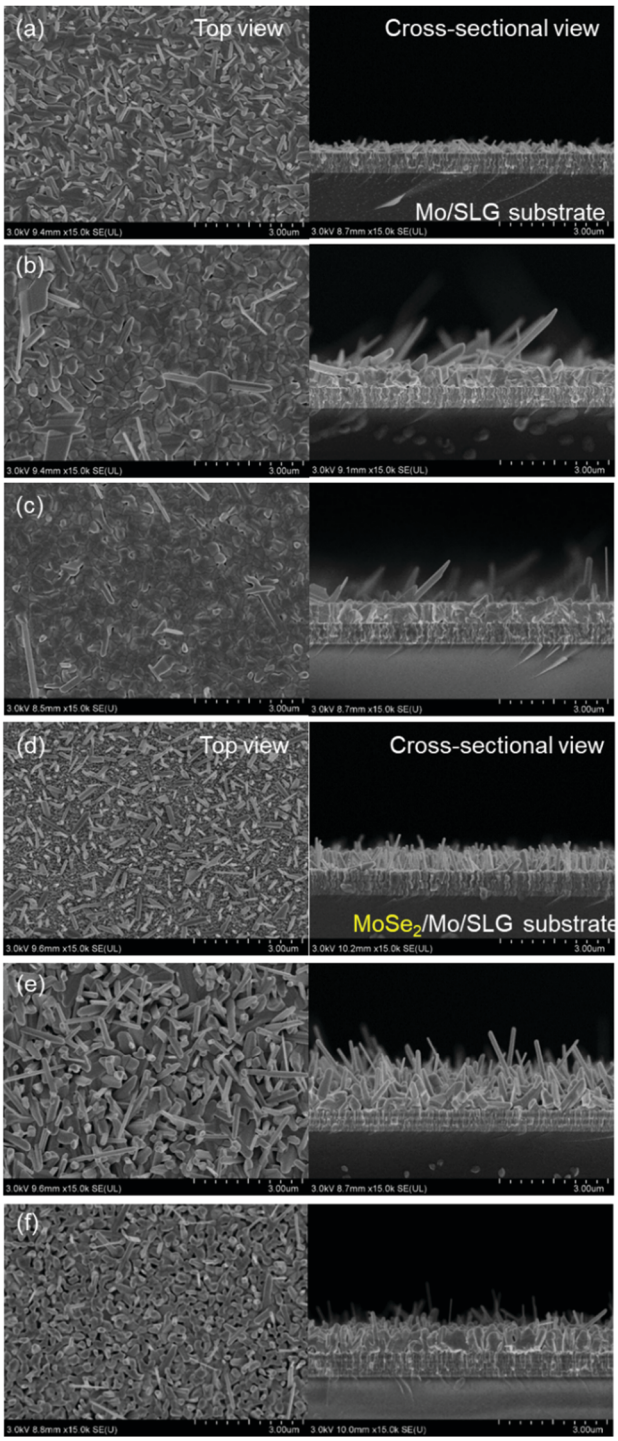

Fig. 1 Top and cross-sectional SEM images of co-evaporated Sb_2Se_3 thin films on bare Mo substrates or $MoSe_2$/Mo substrates at 290 °C and different source evaporation rates: (a), 50 Å s^{-1}; (b), 100 Å s^{-1}; and (c), 200 Å s^{-1} on bare Mo substrates; and (d), 50 Å s^{-1}; (e), 100 Å s^{-1}; and (f), 200 Å s^{-1} on $MoSe_2$/Mo substrates.

the cross-sectional SEM images of Sb_2Se_3 thin films with different substrates and at different evaporation rates.

In the case of co-evaporated Sb_2Se_3 thin films on bare Mo substrates, thin films deposited at a slow source evaporation rate (50 Å s^{-1}) showed a small and randomly oriented Sb_2Se_3 nanorod structure (Fig. 1a). However, as the source evaporation rate increased to 100 Å s^{-1}, Sb_2Se_3 thin films showed a densely packed columnar structure with some long Sb_2Se_3 nanorods (Fig. 1b). At a source evaporation rate of 200 Å s^{-1}, a flat Sb_2Se_3 thin-film structure comprising densely packed grains was observed (Fig. 1c). Generally, the nucleation rate is closely related to the evaporation rate.[26] Thus, a easily formed continuous film under a high evaporation rate was expected. For film materials having an anisotropic crystal structure, such as Sb_2Se_3, rod-shaped film formation is highly probable when the evaporation rate is low. Under these conditions, the impingement rate of adatoms on the substrate decreases and their diffusion length may increase, causing the formation of a non-continuous film. Based on these results, authors believe that controlling the evaporation rate is critical to developing the Sb_2Se_3 rod array for 3D p–n junction solar cells.

Contrary to the co-evaporated Sb_2Se_3 thin films on Mo substrates, Sb_2Se_3 thin films prepared on $MoSe_2$/Mo substrates showed a different nanostructure. All Sb_2Se_3 thin films on $MoSe_2$/Mo substrates showed non-flat thin-film structures, regardless of the source evaporation rate. At an evaporation rate of 50 Å s^{-1}, thin films showed a vertically oriented narrow Sb_2Se_3 nanorod array of length 500 nm (Fig. 1d). The diameter and length of the Sb_2Se_3 nanorods increased with increasing evaporation rate from 50 to 100 Å s^{-1} (Fig. 1e). At an evaporation rate of 200 Å s^{-1}, the thin-film showed ordered arrays of thick Sb_2Se_3 nanorods with a diameter of 100 nm (Fig. 1f). Sb_2Se_3 thin films deposited on $MoSe_2$ substrates showed a Sb_2Se_3 nanorod array structure regardless of the source evaporation rate. Additionally, the Sb_2Se_3 nanorod array nanostructure was tuned by varying the source evaporation rate. The formation of Sb_2Se_3 nanorod array on the $MoSe_2$ interlayer might be attributed to different Sb_2Se_3 crystal growth mechanisms (Fig. 2). Moreover, the $MoSe_2$ interlayer has unique anisotropic structural properties. For example, the (00*l*) plane of $MoSe_2$ has no surface dangling bond, making the nucleation process difficult while facilitating the diffusion and desorption of adatoms on the (00*l*) plane of $MoSe_2$. However, the nucleation process of Sb_2Se_3 could be easily formed on a plane having a high-dangling bond density, such as the one perpendicular to the (00*l*) plane. Therefore, the $MoSe_2$ interlayer was expected to provide a selective nucleation site, facilitating the formation of the Sb_2Se_3 rod array on the $MoSe_2$ interlayer. To investigate in

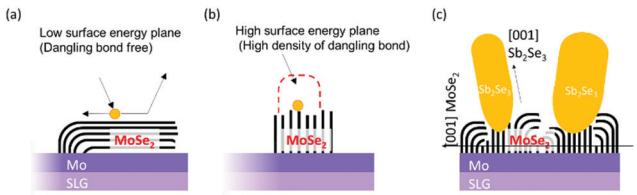

Fig. 2 Schematic diagram of the selective nucleation and growth mechanism of Sb_2Se_3 on the randomly grown $MoSe_2$ interlayer; (a) low surface energy plane, (b) high surface energy plane, and (c) growth of Sb_2Se_3 nanorods on $MoSe_2$ interlayer.

detail the interface between Sb_2Se_3 and $MoSe_2$, a high-angle annular detector dark-field scanning transmission electron microscopy (HADDF-STEM) image of the $Sb_2Se_3/MoSe_2/Mo$ sample was observed (Fig. S3, ESI†). The $MoSe_2$ showed a two-dimensional crystal structure with weak van der Waals bonding forces and without dangling bonds in the *c*-plane of $MoSe_2$. Overall, the layer structure was oriented perpendicular to the Mo substrate. Interestingly, in our case, the density of the $MoSe_2$ interlayer bunch seemed relatively low. Thus, the orientation of the flexible bunch of the $MoSe_2$ layer was not perfectly aligned. The exposed-$MoSe_2$ layer on the surface consisted of a *c*-plane without dangling bonds and another plane with dangling bonds.

To confirm the effect of the substrate type on the morphology of the co-evaporated Sb_2Se_3 thin films, we also deposited Sb_2Se_3 thin films on indium tin oxide (ITO) substrates using the same co-evaporation process. Unlike Mo substrates, all the co-evaporated Sb_2Se_3 thin films on ITO substrates showed a similar dense thin-film morphology, regardless of the source evaporation rate (Fig. S1, ESI†) and substrate temperature (Fig. S2, ESI†). These results show that the type of substrate had a significant effect on the formation of Sb_2Se_3 nanorods by the co-evaporation process.

To evaluate the photovoltaic characteristics of the co-evaporated Sb_2Se_3 thin films on different Mo and $MoSe_2$/Mo substrates, three different Sb_2Se_3 solar cells with a planar device structure of SLG/Mo/$MoSe_2$/Sb_2Se_3/CdS/i-ZnO/AZO/Al were fabricated. Fig. 3 shows the cross-sectional TEM and energy dispersive X-ray spectroscopy (EDS) mapping images of the Sb_2Se_3 solar cells fabricated at different source evaporation rates and with different substrates. The Sb_2Se_3 solar cells without the $MoSe_2$ interlayer showed a planar structure (Fig. 3a and b), due to the flat Sb_2Se_3 thin-film structure shown in Fig. 1c. The CdS buffer, i-ZnO window, and AZO TCO layers were uniformly deposited on the flat Sb_2Se_3 absorber layer. However, the Sb_2Se_3 solar cells prepared on $MoSe_2$/Mo substrates showed completely different nanostructures than those using the Mo substrate. The Sb_2Se_3 absorber layer showed a complex nanorod array, and the CdS buffer layer was deposited on the Sb_2Se_3 nanorods conformally. The ZnO and AZO layers deposited on the rough CdS/Sb_2Se_3 interface showed irregular nanostructures. At the bottom of the Sb_2Se_3 absorber layer, a uniformly formed $MoSe_2$ interlayer was confirmed. Moreover, the source evaporation rate showed a considerable effect on the nanostructure of the Sb_2Se_3 absorber layer. The Sb_2Se_3 solar cells prepared using a 200 Å s^{-1} source evaporation rate on $MoSe_2$/Mo substrates showed an irregular and agglomerated Sb_2Se_3 grain structure (Fig. 3c and d). However, when the evaporation rate decreased to 100 Å s^{-1}, the Sb_2Se_3 absorber layer showed a more ordered and regular nanorod array (Fig. 3e and f). These different Sb_2Se_3 nanorod array structures observed according to the source evaporation rate were consistent with the SEM images (Fig. 1e and f).

Table 1 lists the photovoltaic properties of the Sb_2Se_3 solar cells with and without the $MoSe_2$ interlayer. Despite the planar and uniform device structure of the Sb_2Se_3 solar cells without

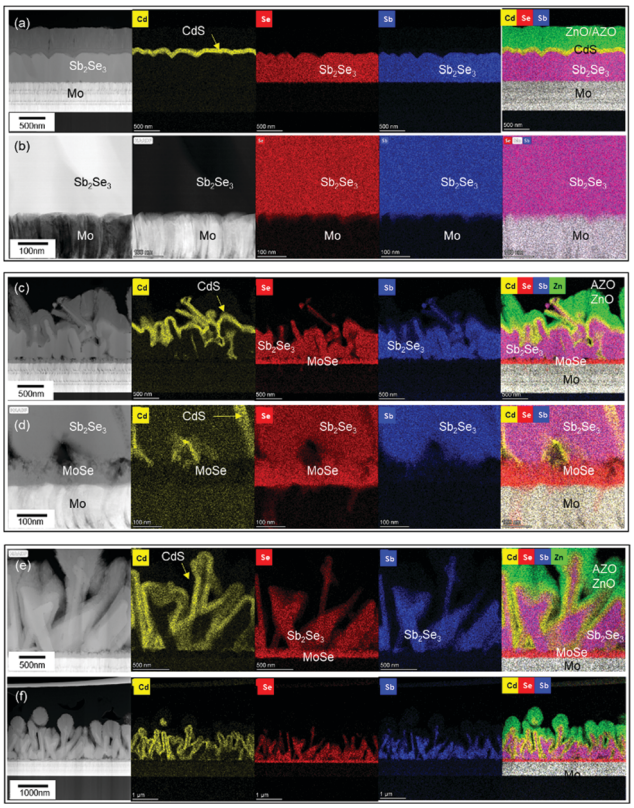

Fig. 3 Cross-sectional TEM and EDS mapping images of Sb_2Se_3 solar cells fabricated with different source evaporation rates and at a temperature of 290 °C. (a) and (b), 200 Å s^{-1} on a Mo substrate; (c) and (d), 200 Å s^{-1} on a $MoSe_2$/Mo substrate; and (e) and (f) 100 Å s^{-1} on a $MoSe_2$/Mo substrate.

the $MoSe_2$ interlayer, the solar cells with the $MoSe_2$ interlayer showed a superior photovoltaic performance. The higher open-circuit voltage (V_{OC}) showed by the Sb_2Se_3 solar cells with the $MoSe_2$ interlayer might be attributed to the quasi-ohmic contact formation between Sb_2Se_3 and $MoSe_2$. The quasi-ohmic contact formation of the $MoSe_2$ interlayer is well known for copper indium gallium diselenide (CIGS) solar cells.[27–31] This quasi-ohmic contact could reduce the contact barrier and series resistance of Sb_2Se_3 solar cell devices. The higher J_{SC} could be related to the 3D p–n junction formation between the Sb_2Se_3 absorber and CdS buffer layers. Due to the 3D p–n junction structure, photo-generated carriers can easily escape into the CdS buffer layer. Thus, nanostructured Sb_2Se_3 solar cells show a higher J_{SC} than flat thin-film Sb_2Se_3 solar cells. This superior photovoltaic performance was consistent with the results reported by Park *et al.* and was also attributed to the 3D p–n junction formation between the Sb_2Se_3 and CdS buffer layers.[17] Between the two Sb_2Se_3 solar cells with a $MoSe_2$ interlayer, the one fabricated at an evaporation rate of 100 Å s^{-1} showed higher J_{SC} and fill factor (FF) than that at 200 Å s^{-1}, which might be attributed to the more regular and ordered 3D p–n junction formation between Sb_2Se_3 and CdS.

A previous report showed that high substrate temperatures induce the evolution of Sb_2Se_3 nanorod arrays, demonstrating the close relationship between the nanostructure of

Table 1 Photovoltaic characteristics of the Sb_2Se_3 solar cells using $MoSe_2$/Mo substrates at 290 °C. Open-circuit voltage (V_{OC}), short-circuit current (J_{SC}), fill factor (FF), power conversion efficiency (PCE), and series and shunt resistances (R_s, R_{sh})

Substrate	Evaporation rate [Å s^{-1}]	V_{OC} [V]	J_{SC} [mA cm^{-2}]	FF [%]	Eff [%]	R_s [Ω cm^2]	R_{sh} [Ω cm^2]
Mo	200	0.20297	8.4189	27.2369	0.465	18.105	26.703
$MoSe_2$/Mo	200	0.43951	21.1832	36.0716	3.358	9.847	51.383
$MoSe_2$/Mo	100	0.44999	23.6606	40.2727	4.288	8.488	70.319

co-evaporated Sb_2Se_3 thin films and substrate temperature.[17] Therefore, we have tried to tune the nanostructure of co-evaporated Sb_2Se_3 thin films by controlling the substrate temperature at a source evaporation rate of 100 Å s^{-1} on $MoSe_2$/Mo substrates. We also prepared co-evaporated Sb_2Se_3 thin films on bare Mo at 315 °C, which is the requirement for Sb_2Se_3 nanorod array formation on bare Mo substrates. Fig. 4 shows the top and cross-sectional SEM images of co-evaporated Sb_2Se_3 thin films at different substrate temperatures on bare Mo or $MoSe_2$/Mo.

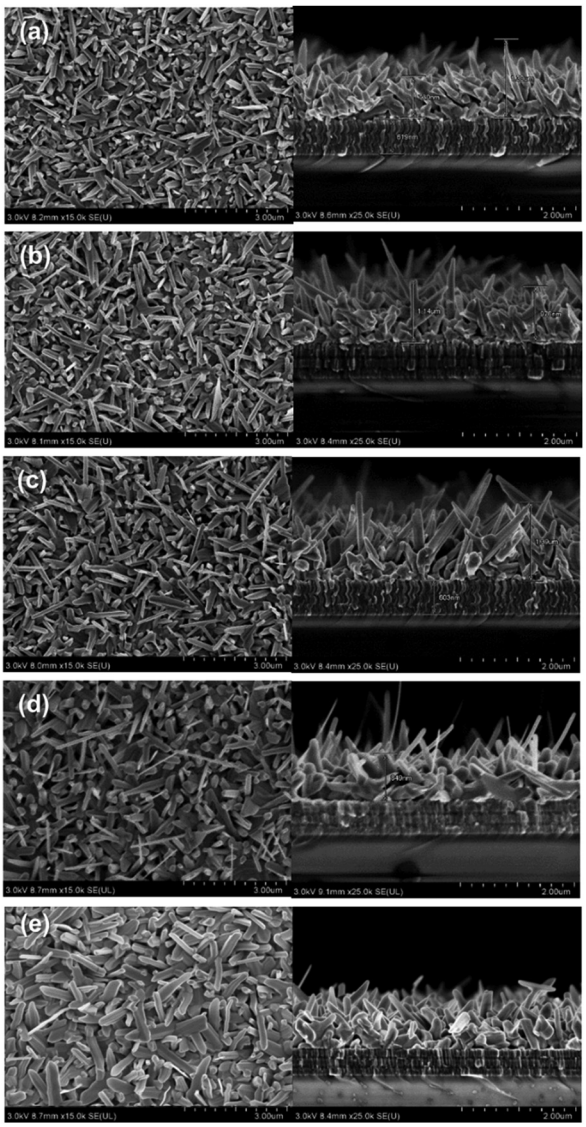

Fig. 4 Top and cross-sectional SEM images of Sb_2Se_3 thin films at a source evaporation rate of 100 Å s^{-1} and different deposition temperatures: (a), 250; (b), 260; (c), 270; and (d), 290 °C using $MoSe_2$/Mo substrates; and (e), 315 °C using a bare Mo substrate.

The co-evaporated Sb_2Se_3 thin films on the $MoSe_2$/Mo substrate did not show the abrupt morphology change, from the flat thin-film structure to a nanorod array, observed in our previous report on Mo substrates.[17] Because the $MoSe_2$ interlayer already easily induces the formation of the Sb_2Se_3 nanorod array, the substrate temperature showed little effect on the formation of the Sb_2Se_3 nanorod array. However, the detailed nanostructure of the Sb_2Se_3 nanorods was affected by the substrate temperature. As the substrate temperature decreased from 290 to 250 °C, the shape regularity and the degree of ordering of the Sb_2Se_3 nanorods improved. As the substrate temperature decreases, the Sb_2Se_3 nuclei density increases, suppressing the rapid growth of Sb_2Se_3 nanorods. Therefore, the growth of Sb_2Se_3 nanorods could be controlled effectively to form an ordered Sb_2Se_3 nanorod array by adjusting the substrate temperature on $MoSe_2$/Mo. Moreover, using the $MoSe_2$ interlayer, it was possible to control the nanostructure of co-evaporated Sb_2Se_3 thin films by varying both the evaporation rate and substrate temperature. Co-evaporated Sb_2Se_3 thin films on a bare Mo substrate at 315 °C also showed a similar Sb_2Se_3 nanorod structure to that on $MoSe_2$/Mo substrates, which is consistent with the results from our previous work.[17] The bare Mo substrate required a higher substrate temperature to form a similar Sb_2Se_3 nanorod array to the one obtained using $MoSe_2$/Mo substrates and the co-evaporation process.

The crystalline orientation of Sb_2Se_3 thin films is well known to be crucial for determining the photovoltaic properties of Sb_2Se_3 solar cells due to the intrinsic one-dimensional ribbon structure of Sb_2Se_3.[32–34] Therefore, the crystalline structure of co-evaporated Sb_2Se_3 thin films on $MoSe_2$/Mo substrate at different substrate temperatures was analyzed by XRD analysis. All the co-evaporated Sb_2Se_3 thin films showed characteristic XRD peaks of Sb_2Se_3. However, the relative intensity of specific peaks corresponding to different crystalline orientations was different for each substrate temperature. Particularly, at 260 °C where the (020) and (120) peaks were not observed, and the intensity of the (211) and (221) peaks increased (Fig. 5a). To further investigate the crystalline orientation of the co-evaporated Sb_2Se_3 thin films, their texture coefficient was calculated.[35–37] At 260 °C the texture coefficient of the (211) peak was remarkably higher than that at other substrate temperatures (Fig. 5b). Additionally, all other Sb_2Se_3 thin films showed relatively higher texture coefficients of ($hk0$) than those at 260 °C. The ($hk1$) preferential orientation of the Sb_2Se_3 thin

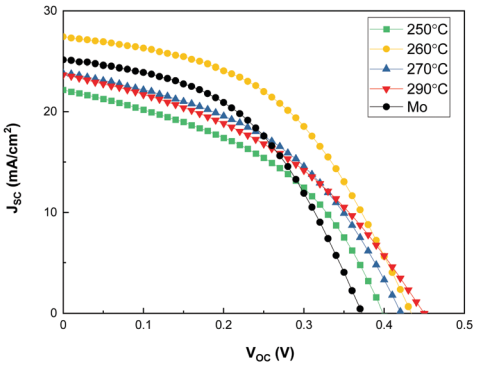

Fig. 5 XRD peaks (a) and texture coefficient (b) of co-evaporated Sb_2Se_3 thin films at different substrate temperatures and at a source evaporation rate of 100 Å s^{-1}.

film at a substrate temperature of 260 °C could help in improving the photovoltaic performance of Sb_2Se_3 solar cells.

Sb_2Se_3 solar cells were fabricated at different substrate temperatures to investigate the effect of substrate temperature of co-evaporated Sb_2Se_3 thin films on their photovoltaic performance. Fig. 6 shows the *I–V* curves of the Sb_2Se_3 solar cells at a source evaporation rate of 100 Å s^{-1} and different substrate temperatures, and Table 2 lists the photovoltaic properties obtained for the Sb_2Se_3 solar cells. All the Sb_2Se_3 solar cells using the $MoSe_2$ interlayer showed a $V_{OC} > 0.4$ V, regardless of the substrate temperature. Because the $MoSe_2$ interlayer already improved the V_{OC}, the structural change in the Sb_2Se_3 nanorods had little effect on the V_{OC}. The Sb_2Se_3 solar cell using a bare Mo substrate showed a slightly lower V_{OC} (0.37 V) than that with $MoSe_2$/Mo substrates. These results show that the introduction of the $MoSe_2$ interlayer significantly improves the V_{OC} of Sb_2Se_3 solar cells. The Sb_2Se_3 solar cell prepared at a substrate temperature of 260 °C showed the highest J_{SC}. This might be attributed to the (*hk*1) preferential orientation of the Sb_2Se_3 absorber layer. Moreover, the ordered and regular Sb_2Se_3 nanorod array could help increase the area of the 3D p–n junction between Sb_2Se_3 and CdS, improving the J_{SC} of the Sb_2Se_3 solar cells. By the way, it showed comparable J_{SC} (25.138 mA cm^{-2}) to those of the Sb_2Se_3 solar cell with $MoSe_2$/Mo substrates because of the densely packed Sb_2Se_3 nanorod array. Interestingly, Sb_2Se_3 solar cells using a

Table 2 Photovoltaic characteristics of the Sb_2Se_3 solar cells using $MoSe_2$/Mo and bare Mo substrates at different temperatures (*T*). Open-circuit voltage (V_{OC}), short-circuit current (J_{SC}), fill factor (FF), power conversion efficiency (PCE), and series and shunt resistances (R_s, R_{sh})

Substrate	Temperature [°C]	V_{OC} [V]	J_{SC} [mA cm^{-2}]	FF [%]	Ef f[%]	R_s [Ω cm^2]	R_{sh} [Ω cm^2]
$MoSe_2$	250	0.40	22.167	43.99	3.886	5.48	67.59
$MoSe_2$	260	0.43	27.430	47.35	5.637	5.89	118.26
$MoSe_2$	270	0.42	23.834	44.47	4.464	6.04	80.89
$MoSe_2$	290	0.45	23.661	40.27	4.288	8.49	70.32
Mo	315	0.37	25.138	47.11	4.412	5.69	112.25

$MoSe_2$/Mo substrate at 250, 270 and 290 °C showed a relatively smaller J_{SC} than bare Mo substrate. The nanostructure changes of the co-evaporated Sb_2Se_3 nanorod array by temperature is remarkable (Fig. 4), which might be closely related to the J_{SC} and FF of Sb_2Se_3 solar cells. At 250 °C, the width of Sb_2Se_3 nanorods is smaller than that at 260 °C, which is disadvantageous for sufficient light absorption. The length uniformity of Sb_2Se_3 nanorods at 270 and 290 °C is inferior compared to that at 260 °C. The irregular nanostructure of the Sb_2Se_3 nanorods induces insufficient light absorption and photo-generated carrier transportation. The thinner rods (250 °C) and increased empty space (270 °C) could deteriorate the FF by increasing the shunt paths too.

To investigate the correlation between the 3D p–n junction structure and the photovoltaic properties of Sb_2Se_3 solar cells, TEM analysis of the best Sb_2Se_3 solar cell, with the evaporation rate of 100 Å s^{-1} and the substrate temperature of 260 °C, was performed. Fig. 7 shows the TEM-EDS mapping images of the Sb_2Se_3 solar cell device with a nanorod array with a PCE of 5.637% (Table 2). The Sb_2Se_3 solar cell using a $MoSe_2$/Mo substrate showed a 1.225% higher PCE than the one using a bare Mo substrate, which might be attributed to the improved V_{OC}. A densely packed, uniformly distributed, Sb_2Se_3 nanorod array and the 3D p–n junction between CdS and Sb_2Se_3 nanorods were observed. These properties are advantageous for the enhancement of J_{SC}. Additionally, the uniform $MoSe_2$ interlayer between the Mo substrate and the Sb_2Se_3 nanorod array is beneficial for the formation of a quasi-ohmic contact between the layers.

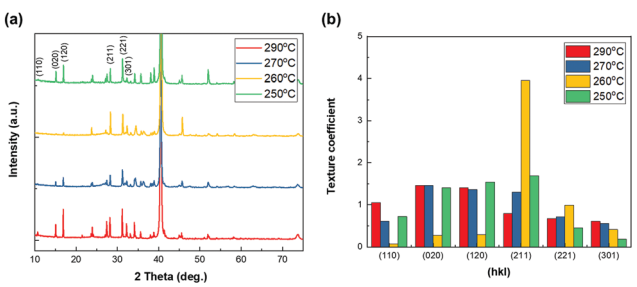

Fig. 6 *I–V* curves of Sb_2Se_3 solar cells at a source evaporation rate of 100 Å s^{-1} and different substrate temperatures: (a), 250; (b), 260; (c), 270; and (d), 290 °C using $MoSe_2$/Mo and bare Mo substrates.

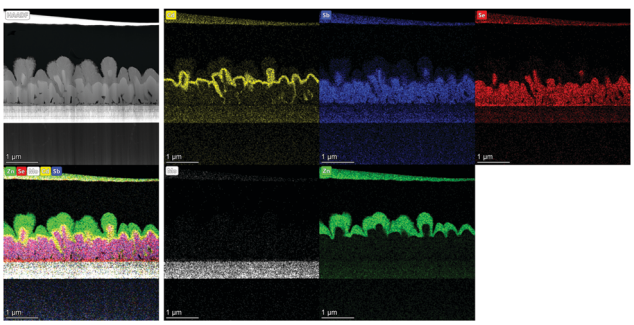

Fig. 7 STEM-EDS mapping images of Sb_2Se_3 nanorod array solar cell with PCE of 5.637%.

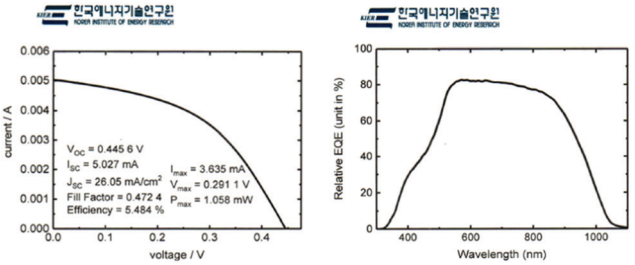

Fig. 8 Certified J–V curve (a) and external quantum efficiency (EQE) data (b) of Sb_2Se_3 solar cells at a substrate temperature of 260 °C and a source evaporation rate of 100 Å s^{-1} using a $MoSe_2$/Mo substrate (Korea Institute of Energy Research, KIER).

The results presented in this work reveal that the $MoSe_2$ interlayer between a Mo substrate and a Sb_2Se_3 absorber layer improves the performance of Sb_2Se_3 solar cells in two relevant ways. First, the contact quality between Sb_2Se_3 and Mo layers improved due to quasi-ohmic contact formation, which was confirmed by the higher V_{OC} values of Sb_2Se_3 solar cells using $MoSe_2$/Mo substrates compared to those using a bare Mo substrate; second, a facile formation of the Sb_2Se_3 nanorod array and a lower substrate temperature were achieved using the co-evaporation process, which was followed by the 3D p–n junction Sb_2Se_3 solar cell fabrication. Moreover, the $MoSe_2$ interlayer played a key role in improving the photovoltaic performance of the Sb_2Se_3 nanorod array solar cell by increasing both V_{OC} and J_{SC}. The quasi-ohmic contact caused by the $MoSe_2$ interlayer effectively improved the contact quality between Sb_2Se_3 layers and Mo substrates. Moreover, the $MoSe_2$ interlayer also played a critical role as a seed layer for the uniform growth of the Sb_2Se_3 nanorod array.

The Sb_2Se_3 solar cells prepared by co-evaporation at a source evaporation rate of 100 Å s^{-1} and substrate temperature of 260 °C on a $MoSe_2$/Mo substrate were analyzed by an external certified laboratory to verify our PCE laboratory measurements. The certified J–V curve (Fig. 8a) and external quantum efficiency data (Fig. 8b) showed similar results (PCE of 5.484%) to our lab-scale photovoltaic measurements. We calculated integrated J_{SC} from EQE data and compared with the J_{SC} of J–V curve. The J_{SC} from integrated EQE (25.89 mA cm^{-2}) is similar to the J_{SC} of the J–V curve (26.05 mA cm^{-2}).

Conclusions

This work investigated the role of the $MoSe_2$ interlayer on the growth of the Sb_2Se_3 nanorod array and the contact quality between Sb_2Se_3 thin films and Mo substrates. By introducing a $MoSe_2$ interlayer between Sb_2Se_3 layers and Mo substrates, uniformly ordered densely packed Sb_2Se_3 nanorods were successfully prepared. The $MoSe_2$ interlayer, with locally distributed high surface energy planes, played a crucial role as a seed layer for the preferential growth of Sb_2Se_3 crystals perpendicular to the substrate, which facilitated the formation of a Sb_2Se_3 nanorod array on the $MoSe_2$ interlayer. The latter also significantly improved the photovoltaic performance of Sb_2Se_3 solar cell devices by forming a quasi-ohmic contact between Sb_2Se_3 absorber layers and Mo substrates, resulting in higher V_{OC} and J_{SC}. The nanostructure and crystalline orientation of the Sb_2Se_3 nanorods array were affected by the substrate temperature and the source evaporation rate during the co-evaporation process. 3D p–n junction solar cells based on an ordered and (*hk*1) preferentially oriented Sb_2Se_3 nanorods array showed a PCE of 5.637%.

Conflicts of interest

There are no conflicts to declare.

Acknowledgements

This work was supported by the DGIST R & D Programs of the Ministry of Science and ICT, Republic of Korea (21-CoE-ET-01, 21-ET-08). We thank Mr Eun and Mr Cheon at the Center for Core Research Facilities (CCRF) of DGIST for FIB sampling and STEM measurements.

Notes and references

1 Y. Zhou, M. Y. Leng, Z. Xia, J. Zhong, H. B. Song, X. S. Liu, B. Yang, J. P. Zhang, J. Chen, K. H. Zhou, J. B. Han, Y. B. Cheng and J. Tang, *Adv. Energy Mater.*, 2014, **4**, 1301846.
2 G. X. Liang, Z. H. Zheng, P. Fan, J. T. Luo, J. G. Hu, X. H. Zhang, H. L. Ma, B. Fan, Z. K. Luo and D. P. Zhang, *Sol. Energy Mater. Sol. Cells*, 2018, **174**, 263–270.
3 C. C. Yuan, L. J. Zhang, W. F. Liu and C. F. Zhu, *Sol. Energy*, 2016, **137**, 256–260.
4 M. Birkett, W. M. Linhart, J. Stoner, L. J. Phillips, K. Durose, J. Alaria, J. D. Major, R. Kudrawiec and T. D. Veal, *APL Mater.*, 2018, **6**, 84901.
5 X. M. Wang, R. F. Tang, C. Y. Wu, C. F. Zhu and T. Chen, *J. Energy Chem.*, 2018, **27**, 713–721.
6 K. Shen, C. Z. Ou, T. L. Huang, H. B. Zhu, J. J. Li, Z. Q. Li and Y. Mai, *Sol. Energy Mater. Sol. Cells*, 2018, **186**, 58–65.
7 S. Chen, T. Liu, Z. Zheng, M. Ishaq, G. Liang, P. Fan, T. Chen and J. Tang, *J. Energy Chem.*, 2022, **67**, 508–523.
8 P. Fan, G. J. Chen, S. Chen, Z. H. Zheng, M. Azan, N. Ahmad, Z. H. Su, G. X. Liang, X. H. Zhang and Z. G. Chen, *ACS Appl. Mater. Interfaces*, 2021, **13**, 46671–46680.
9 G. X. Liang, Y. D. Luo, S. Chen, R. Tang, Z. H. Zheng, X. J. Li, X. S. Liu, Y. K. Liu, Y. F. Li, X. Y. Chen, Z. H. Su and X. H. Zhang, *Nano Energy*, 2020, **73**, 104806.
10 Y. D. Luo, R. Tang, S. Chen, J. G. Hu, Y. K. Liu, Y. F. Li, X. S. Liu, Z. H. Zheng, Z. H. Su, X. F. Ma, P. Fan, X. H. Zhang, H. L. Ma, Z. G. Chen and G. X. Liang, *Chem. Eng. J.*, 2020, **393**, 124599.
11 R. Tang, S. Z. H. Zheng, Z. H. Su, X. J. Li, Y. D. Wei, X. H. Zhang, Y. Q. Fu, J. T. Luo, P. Fan and G. X. Liang, *Nano Energy*, 2019, **64**, 103929.
12 R. F. Tang, X. M. Wang, W. T. Lian, J. L. Huang, Q. Wei, M. L. Huang, Y. W. Yin, C. H. Jiang, S. F. Yang, G. C. Xing,

S. Y. Chen, C. F. Zhu, X. J. Hao, M. A. Green and T. Chen, *Nat. Energy*, 2020, **5**, 587–595.
13 P. V. Kamat, K. Tvrdy, D. R. Baker and J. G. Radich, *Chem. Rev.*, 2010, **110**, 6664–6688.
14 M. Yu, Y. Z. Long, B. Sun and Z. Y. Fan, *Nanoscale*, 2012, **4**, 2783–2796.
15 W. Yang, J. Ahn, Y. Oh, J. Tan, H. Lee, J. Park, H. C. Kwon, J. Kim, W. Jo, J. Kim and J. Moon, *Adv. Energy Mater.*, 2018, **8**, 1702888.
16 Z. Q. Li, X. Y. Liang, G. Li, H. X. Liu, H. Y. Zhang, J. X. Guo, J. W. Chen, K. Shen, X. Y. San, W. Yu, R. E. I. Schropp and Y. H. Mai, *Nat. Commun.*, 2019, **10**, 125.
17 S. N. Park, S. Y. Kim, S. J. Lee, S. J. Sung, K. J. Yang, J. K. Kang and D. H. Kim, *J. Mater. Chem. A*, 2019, **7**, 25900–25907.
18 Z. Li, X. Chen, H. Zhu, J. Chen, Y. Guo, C. Zhang, W. Zhang, X. Niu and Y. Mai, *Sol. Energy Mater. Sol. Cells*, 2017, **161**, 190–196.
19 Y. H. Kwon, Y. B. Kim, M. Jeong, H. W. Do, H. K. Cho and J. Y. Lee, *Sol. Energy Mater. Sol. Cells*, 2017, **172**, 11–17.
20 L. Wang, D. B. Li, K. H. Li, C. Chen, H. X. Deng, L. Gao, Y. Zhao, F. Jiang, L. Y. Li, F. Huang, Y. S. He, H. S. Song, G. D. Niu and J. Tang, *Nat. Energy*, 2017, **2**, 17046.
21 C. Chen, L. Wang, L. Gao, D. Nam, D. B. Li, K. H. Li, Y. Zhao, C. Ge, H. Cheong, H. Liu, H. S. Song and J. Tang, *ACS Energy Lett.*, 2017, **2**, 2125–2132.
22 O. S. Hutter, L. J. Phillips, K. Durose and J. D. Major, *Sol. Energy Mater. Sol. Cells*, 2018, **188**, 177–181.
23 C. Chen, K. H. Li, S. Y. Chen, L. Wang, S. C. Lu, Y. H. Liu, D. B. Li, H. S. Song and J. Tang, *ACS Energy Lett.*, 2018, **3**, 2335–2341.
24 X. X. Wen, C. Chen, S. C. Lu, K. H. Li, R. Kondrotas, Y. Zhao, W. H. Chen, L. Gao, C. Wang, J. Zhang, G. D. Niu and J. Tang, *Nat. Commun.*, 2018, **9**, 2179.
25 K. H. Li, S. Y. Wang, C. Chen, R. Kondrotas, M. C. Hu, S. C. Lu, C. Wang, W. Chen and J. Tang, *J. Mater. Chem. A*, 2019, **7**, 9665–9672.
26 M. Ohring, in *Materials Science of Thin Films*, ed. M. Ohring, Academic Press, San Diego, 2nd edn, 2002, pp. 357–415, DOI: 10.1016/B978-012524975-1/50010-0.
27 H.-y. Sun, P.-h. Li, Y.-m. Xue, Z.-x. Qiao and L. Sai, *Optoelectron. Lett.*, 2019, **15**, 428–434.
28 L. Assmann, J. C. Bernede, A. Drici, C. Amory, E. Halgand and M. Morsli, *Appl. Surf. Sci.*, 2005, **246**, 159–166.
29 N. Kohara, S. Nishiwaki, Y. Hashimoto, T. Negami and T. Wada, *Sol. Energy Mater. Sol. Cells*, 2001, **67**, 209–215.
30 J. Chantana, T. Kato, H. Sugimoto and T. Minemoto, *Appl. Phys. Lett.*, 2018, **112**, 151601.
31 S. Nishiwaki, N. Kohara, T. Negami and T. Wada, *Jpn. J. Appl. Phys.*, 1998, **37**, L71–L73.
32 Y. Zhou, L. Wang, S. Y. Chen, S. K. Qin, X. S. Liu, J. Chen, D. J. Xue, M. Luo, Y. Z. Cao, Y. B. Cheng, E. H. Sargent and J. Tang, *Nat. Photonics*, 2015, **9**, 409–415.
33 Z. Q. Li, H. B. Zhu, Y. T. Guo, X. N. Niu, X. Chen, C. Zhang, W. Zhang, X. Y. Liang, D. Zhou, J. W. Chen and Y. H. Mai, *Appl. Phys. Express*, 2016, **9**, 052302.
34 X. S. Liu, J. Chen, M. Luo, M. Y. Leng, Z. Xia, Y. Zhou, S. K. Qin, D. J. Xue, L. Lv, H. Huang, D. M. Niu and J. Tang, *ACS Appl. Mater. Interfaces*, 2014, **6**, 10687–10695.
35 S. Dias, B. Murali and S. B. Krupanidhi, *Sol. Energy Mater. Sol. Cells*, 2015, **143**, 152–158.
36 S. Karim, M. E. Toimil-Molares, F. Maurer, G. Miehe, W. Ensinger, J. Liu, T. W. Cornelius and R. Neumann, *Appl. Phys. A: Mater. Sci. Process.*, 2006, **84**, 403–407.
37 Y. Q. Wang, W. Tang and L. Zhang, *J. Mater. Sci. Technol.*, 2015, **31**, 175–181.